

# The Chandra view of the Largest Quasar Lens SDSS J1029+2623

Naomi Ota,<sup>1</sup> Masamune Oguri,<sup>2</sup> Xinyu Dai,<sup>3</sup> Christopher S. Kochanek,<sup>4</sup> Gordon T. Richards,<sup>5</sup> Eran O. Ofek,<sup>6</sup> Roger D. Blandford,<sup>7</sup> Tim Schrabback,<sup>8</sup> and Naohisa Inada<sup>9</sup>

Received \_\_\_\_\_; accepted \_\_\_\_\_

Submitted to ApJ

---

<sup>1</sup>Department of Physics, Nara Women's University, Kita-uoyanishimachi, Nara, Nara 630-8506, Japan.

<sup>2</sup>Institute for the Physics and Mathematics of the Universe, University of Tokyo, 5-1-5 Kashiwa-no-ha, Kashiwa, Chiba 277-8568, Japan.

<sup>3</sup>Homer L. Dodge Department of Physics and Astronomy, University of Oklahoma, Norman, OK 73019, USA.

<sup>4</sup>Department of Astronomy, The Ohio State University, Columbus, OH 43210, USA.

<sup>5</sup>Department of Physics, Drexel University, 3141 Chestnut Street, Philadelphia, PA 19104, USA.

<sup>6</sup>Ben-Ziyo Center for Astrophysics, Weizmann Institute of Science, 76100 Rehovot, Israel.

<sup>7</sup>Kavli Institute for Particle Astrophysics and Cosmology, 2575 Sand Hill Rd., Menlo Park, CA 94309, USA.

<sup>8</sup>Kavli Institute for Particle Astrophysics and Cosmology, Stanford University, 382 Via Pueblo Mall, Stanford, CA 94305-4060, USA

<sup>9</sup>Department of Physics, Nara National College of Technology, Yamatokohriyama, Nara 639-1080, Japan.

## ABSTRACT

We present results from *Chandra* observations of the  $z_l = 0.58$  cluster lens SDSS J1029+2623, which is presently the largest separation gravitationally lensed quasar. We clearly detect X-ray emission both from the lensing cluster and the three lensed quasar images. The cluster has an X-ray temperature of  $kT = 8.1^{+2.0}_{-1.2}$  keV and luminosity  $L_X = 9.6 \times 10^{44}$  erg s $^{-1}$ . Its surface brightness is centered near galaxy G2 and it is elongated East-West. We identify a subpeak North-West of the main peak, which is suggestive of an ongoing merger. Even so, the X-ray mass inferred from the hydrostatic equilibrium assumption appears to be consistent with the Einstein radius of the system. We find significant absorption in the soft X-ray spectrum of quasar image C, which can be caused by an intervening material at either the lens or source redshift. The X-ray flux ratios between the quasar images after correcting for absorption are in reasonable agreement with those at optical and radio wavelengths. This implies that microlensing effect is not significant for this system and dark matter substructure is mainly responsible for the anomalous flux ratios.

*Subject headings:* galaxies: clusters: general — gravitational lensing: strong — quasars: individual (SDSS J1029+2623) — X-rays: galaxies

## 1. Introduction

The gravitational lens SDSS J1029+2623 consists of three images of a  $z_s = 2.197$  quasar produced by a foreground cluster at  $z_l \approx 0.58$  (Inada et al. 2006; Oguri et al. 2008). With a maximum image separation of  $22''.5$ , this is the largest lens among  $\sim 130$  gravitationally lensed quasars known to date. The lensing interpretation is secure from multiple observational facts, including the remarkably similar optical spectra with mini broad absorption line (BAL) features in their emission lines, similar radio loudnesses (Kratzer et al. 2011), and the identification of the lensing cluster in the optical and with weak lensing (Oguri et al. 2012). Furthermore, this lens system represents a rare example of a naked cusp lens. In this configuration, only three images with similar brightnesses are produced on the same side of the lens potential, which has been predicted to be fairly common among cluster-scale lenses (Oguri & Keeton 2004; Li et al. 2007; Minor & Kaplinghat 2008).

SDSS J1029+2623 is one of two examples of large-separation quasar lenses produced by massive clusters of galaxies. The other large-separation lens is SDSS J1004+4112 (Inada et al. 2003; Oguri et al. 2004; Sharon et al. 2005; Inada et al. 2005). In fact, these clusters can be regarded as unique examples of *strong-lens-selected* clusters in the sense that they have been identified by searching for strong lenses in a large sample of quasars. Therefore, detailed studies of the lensing clusters may provide useful insights into the nature and diversity of intermediate redshift clusters. In particular, (1) do the strong-lens-selected clusters follow empirical scaling relations derived from optical/X-ray selected clusters? and (2) what is the dynamical state of these clusters?

*Chandra* and *XMM-Newton* observations of the other large-separation quasar lens, SDSS J1004+4112, have shown that the lensing cluster is relaxed, with the X-ray temperature and luminosity being consistent with the predictions of empirical scaling

relations within the observed scatter (Ota et al. 2006b; Lamer et al. 2006). This interpretation is also supported by the recent comparison of the X-ray measurements with detailed strong lens models (Oguri 2010). There is excellent agreement on the centroids and position angles between the inferred dark matter distribution, the X-ray surface brightness, and the brightest cluster galaxy.

The available observational data suggest that the lensing cluster of SDSS J1029+2623 may be quite complicated. For instance, the existence of two bright elliptical galaxies at the center with a large velocity difference ( $\sim 2800 \text{ km s}^{-1}$ ) between them indicates a possible merger. High-resolution *Chandra* imaging and spectroscopy are essential for studying the dynamical state of the lensing cluster, based on detailed comparisons between the gas distribution probed by the X-ray measurements and the mass distribution obtained from strong and weak lensing (e.g., Clowe et al. 2006).

In addition to the properties of the lensing cluster, the high-resolution *Chandra* observations provide an additional probe of the anomalous flux ratio between the quasar images. In particular, the large flux difference between the close quasar image pair (images B and C) is observed in the radio (Kratzer et al. 2011), which implies that a large part of the flux anomaly is caused by (sub-)structure in the mass distribution of the lensing cluster. However, there is a clear wavelength dependence to the optical flux ratios (Oguri et al. 2008), which indicates that chromatic microlensing or dust extinction must also affect the third quasar image.

In this paper, we present results from *Chandra* observations of this unique cluster-scale quasar lens. We successfully detected X-ray emission from both the lensing cluster and the three quasar images, which are discussed in §3 and §4, respectively. We compare our results with observations at other wavelengths, as well as strong lensing information from the quasar images. Throughout the paper we adopt a cosmological model with matter density

$\Omega_M = 0.27$ , cosmological constant  $\Omega_\Lambda = 0.73$ , and Hubble constant  $H_0 = 70 \text{ km s}^{-1} \text{ Mpc}^{-1}$ . At the cluster redshift of  $z = 0.584$ ,  $1''$  corresponds to 6.69 kpc. Unless otherwise specified, quoted errors indicate the 90% confidence range.

## 2. Observations

SDSS J1029+2623 was observed for 60 ks with the *Chandra* Advanced CCD Imaging Spectrometer (ACIS; Garmire et al. 2003) on 2010 March 11 (Observation ID: 11755). The data were obtained with the ACIS S3 CCD operating in VFaint mode. This CCD has a  $1024 \times 1024$  pixel format with an image scale of  $0''.492 \text{ pixel}^{-1}$ . The target was offset from the nominal aim point with a Y-offset of  $-1'$ , which has little effect on the spatial resolution. The CCD temperature during the observations was  $-120^\circ\text{C}$ . The data were processed using the standard software packages CIAO 4.3 and CALDB 4.4.1. The background was stable during the observation and the net exposure time after applying standard light-curve screening cuts was 55815 s.

The ACIS image in the 0.5–7 keV band is shown in Figure 1. The extended cluster emission and the three images of SDSS J1029+2623 are all detected. The astrometry offset is found to be negligibly small ( $0''.2$ ) from the comparison of quasar A position with the optical image. The cluster emission exhibits a somewhat elongated feature, which we will study in detail in §3.2. In the ACIS-S3 field, 42 point-like sources, including the three quasar images, were detected with the `wavdetect` algorithm for a significance threshold parameter of  $10^{-6}$ . The X-ray centroid position (10:29:12.47, +26:23:33.2), measured in §3.2, agrees well with the position of the central galaxy G2 at (10:29:12.48, +26:23:32.0; Inada et al. 2006).

### 3. Lensing cluster

#### 3.1. Spectral analysis

We derive the spectrum of the cluster component by extracting the data from a circular region with a radius of  $1'$  centered on the X-ray centroid. We exclude  $5''$  radius regions around each quasar image. The background was estimated in a surrounding annulus ( $2'.2 < r < 2'.5$ ). The source count rate within  $r < 1'$  is  $0.068 \pm 0.001 \text{ counts s}^{-1}$ . We fit the cluster spectrum in the 0.5–7 keV band with the APEC thin-thermal plasma model (Smith et al. 2001) utilizing XSPEC version 12.6.0q. The Galactic hydrogen column density was fixed to  $N_{\text{H}} = 1.67 \times 10^{20} \text{ cm}^{-2}$  based on the LAB survey (Kalberla et al. 2005). Given the good agreement between the X-ray emission centroid and the position of G2 galaxy (see below), we set the cluster redshift to that of G2 ( $z = 0.584$ ; Oguri et al. 2008).

The spectrum is shown in Figure 2. From the spectral fits the X-ray temperature is constrained to be  $kT = 8.1_{-1.2}^{+2.0} \text{ keV}$  and the metal abundance to be  $Z = 0.21Z_{\odot}$  (the 90% upper limit is  $0.44Z_{\odot}$ ). This high temperature indicates that the lensing cluster is indeed massive enough to be capable of producing the large-separation lensed quasar images. The reduced chi-square of the best-fit model is  $\chi^2/\text{dof} = 138/139$ , and the parameters of the fit are summarized in Table 1.

The absorption-corrected 0.5–7 keV flux is  $4.6 \times 10^{-13} \text{ erg s}^{-1}$  ( $r < 1'$ ). The bolometric X-ray luminosity within  $r_{500}$  is estimated as  $L_{\text{X}} = 9.6 \times 10^{44} \text{ erg s}^{-1}$ , where  $r_{500}$  is defined as the radius within which the average matter density is equal to  $\Delta_c = 500$  times the critical density of the Universe at the cluster redshift. The  $\beta$ -model analysis in § 3.2 yields  $r_{500} = 1.09 \text{ Mpc}$ . This luminosity is lower than the mean value expected from the luminosity-temperature relation of distant clusters,  $L_{\text{X}} = 4.0 \times 10^{45} \text{ erg s}^{-1}$  (Ota et al. 2006a), but it is within the observed scatter of the  $L_{\text{X}} - T$  relation.

To investigate the radial temperature profile, we also analyze spectra for the inner  $r < 0'.25$  ( $\sim 100$  kpc) region and the outer  $0'.25 < r < 1'$  region of the lensing cluster. The fitted temperatures are  $kT = 9.8^{+3.7}_{-2.1}$  keV and  $6.8^{+1.7}_{-1.2}$  keV, respectively. While the temperature profile is consistent with being constant with radius, the possible decrease of the temperature toward large radii implies that the lensing cluster lacks the radiatively cooling core commonly seen in unrelaxed clusters (Arnaud et al. 2010).

### 3.2. Image analysis

We first fit a single one-dimensional radial surface-brightness profiles to the extended X-ray emission. We centered the models at the X-ray centroid and azimuthally averaged the 0.5–5 keV image. We corrected for vignetting and the detector response using the exposure map calculated for the spectral energy distribution of the cluster. The image was rebinned by a factor of two so that the pixel scale is  $0''.98$  (6.58 kpc at the cluster redshift). The quasar images were masked out to  $5''$  when calculating the profile.

We fit the radial profile with the following two models: (1) the conventional  $\beta$ -model  $S(r) = S_0[1 + (r/r_c)^2]^{-3\beta+1/2}$ , and (2) the profile derived from the universal mass profile proposed by Navarro et al. (1997) plus isothermality of the cluster (Suto et al. 1998, hereafter NFW-SSM). The background level, which was assumed to be a constant, is simultaneously fit. As illustrated in Figure 3, we find that both models can fit the observed radial profile reasonably well, with reduced chi-square values of  $\chi^2/\text{dof} = 183.2/196$  and  $178.9/196$  for the  $\beta$ -model and NFW-SSM model, respectively. The fitted values of the  $\beta$ -model parameters are  $\beta = 0.72^{+0.05}_{-0.04}$  and  $r_c = 16.4^{+1.8}_{-1.6}$  arcsec ( $= 109^{+12}_{-11}$  kpc), while the NFW-SSM model parameters are  $B = 12.2^{+1.6}_{-1.2}$  and  $r_s = 78^{+16}_{-11}$  arcsec ( $= 519^{+104}_{-77}$  kpc).

In the  $\beta$ -model, the central electron density is  $n_{e0} = (1.5 \pm 0.1) \times 10^{-2} \text{ cm}^{-3}$ . This

implies a radiative cooling time at the cluster center of  $t_{\text{cool}} = 5.8_{-0.9}^{+1.1}$  Gyr, which is shorter than the Hubble time but comparable to the age of the Universe at the cluster redshift,  $t_{\text{age}} = 8.2$  Gyr. Radiative cooling should not be important in the cluster core region.

The *Chandra* image suggests that the cluster emission is somewhat elongated along the East-West direction. Moreover, there is another emission peak about  $10''$  North-West of the cluster centroid (Fig. 1). These motivate us to explore the X-ray surface brightness with two-dimensional models, adopting both the single- and double-component elliptical  $\beta$ -models. The elliptical  $\beta$ -model<sup>1</sup> is defined by

$$\begin{aligned} S(x, y) &= S_0 \left[ 1 + \left( \frac{r}{r_c} \right)^2 \right]^{-3\beta+1/2} + C, \\ r(x, y) &= \left[ \{(x - x_0) \cos \theta + (y - y_0) \sin \theta\}^2 (1 - \epsilon)^2 \right. \\ &\quad \left. + \{(y - y_0) \cos \theta - (x - x_0) \sin \theta\}^2 \right]^{1/2} / (1 - \epsilon), \end{aligned} \quad (1)$$

where  $r_c$  is the core radius,  $x_0$  and  $y_0$  define the cluster center,  $\epsilon$  is the ellipticity,  $\theta$  is the position angle,  $S_0$  is the amplitude at the center. The background level per image pixel was fixed to the value obtained from the one-dimensional analysis,  $C = 3.3 \times 10^{-9} \text{ counts s}^{-1} \text{ cm}^{-2}$ .

We first fit a single-component elliptical  $\beta$ -model. The maximum-likelihood fit was performed with **Sherpa**, where the exposure map was included to convolve the model image with the telescope and detector responses. We find that the fit residuals show significant excess emission in the North-West region, as shown in Fig. 4. The parameters and results for the single-component model are summarized in Table 3.

We next consider a two-component model in order to determine the X-ray emission profile of the ICM more precisely. The model consists of two elliptical  $\beta$ -models, one

---

<sup>1</sup>beta2d model in the **Sherpa** fitting package



centered on the cluster and the other on the North-West component, plus the constant background. For the North-West component, the parameter  $\beta_2$  and position angle  $\theta_2$  were fixed to 0.7 and 0, respectively, due to the limited photon statistics. The results from fitting the central  $3'3 \times 3'3$  region are shown in Table 3 and Figure 5. In order to check the goodness of the fit, we re-binned the image into two single-dimensional profiles in the Right Ascension and Declination directions (Fig. 5, bottom right) and calculated the  $\chi^2$  values between the model and data profiles within the central  $\pm 1'$  region to find that they are sufficiently small,  $\chi^2/\text{dof} = 131/122$  and  $148/122$  for the  $x$ - and  $y$ -directions, respectively. The best-fit cluster-center position of (10:29:12.47, +26:23:33.2) is consistent with G2 (10:29:12.48, +26:23:32.0; Inada et al. 2006) within the errors. The ellipticity of the main cluster component is measured to be  $\epsilon = 0.214^{+0.034}_{-0.035}$  (axis ratio  $q = 0.786$ ), which is quite typical of X-ray surface brightness ellipticities (De Filippis et al. 2005; Flores et al. 2007; Hashimoto et al. 2007; Kawahara 2010; Lau et al. 2012).

Note that there appears to be no optical counterpart for the NW peak at (10:29:11.9, +26:23:37.4). For the APEC model, the X-ray spectrum extracted from  $r < 5''$  around the NW peak with subtracted background from the surrounding  $5'' < r < 10''$  region yields  $kT = 3.8(> 1.7)$  keV and an unabsorbed bolometric luminosity of  $1.5 \times 10^{43} \text{ erg s}^{-1}$ . Adopting the estimated bolometric luminosity, a temperature of 1.1 keV is obtained from the luminosity-temperature relation for such small core radius clusters (Ota et al. 2006a), which is significantly lower than the temperature measured from the *Chandra* observation. This might be the signature that the NW component is in the process of merging with the main cluster or has recently undergone a merger. These parameters are reminiscent of the emission peak detected in the line-of-sight merging system CL0024+17 (Ota et al. 2004). In addition, there is a possible jump in the X-ray surface brightness distribution near the NW peak (Fig. 1). These observed features suggest that the NW peak may be a cold front (Markevitch et al. 2000; Owers et al. 2009), although the limited photon statistics prevent

a more detailed exploration.

### 3.3. Cluster mass distribution

Under the assumption of hydrostatic equilibrium and spherical symmetry, we can infer the mass distribution of the lensing cluster from the X-ray temperature and surface-brightness profiles. We assume isothermality because we did not detect a significant radial dependence of the X-ray temperature. Figure 6 shows the cylindrical cluster mass projected within a radius  $r$  derived from each surface mass distribution profile. We find that both models yield consistent mass profiles within the measurement errors.

For the NFW-SSM model and the critical overdensity  $\Delta_c = \Delta_{\text{vir}} = 18\pi^2\Omega^{0.427}$  (Nakamura & Suto 1997), the virial mass and the concentration parameter are constrained to be  $M_{\text{vir}} = 1.57_{-0.39}^{+0.66} \times 10^{15} M_{\odot}$  and  $c_{\text{vir}} = 4.52_{-0.58}^{+0.58}$ . However, these values should be taken with caution because they rely on the extrapolation of the profiles well beyond the radii where X-ray properties are measured. For comparison with other mass measurements, it may be better to use masses defined for larger critical overdensities  $\Delta_c$ . In Table 4 we summarize the mass and radius estimated for the virial overdensity and overdensities of  $\Delta_c = 500, 1000$ , and  $2500$ , for both the  $\beta$ -model and the NFW-SSM model.

Next we compare the mass distribution derived from the X-ray analysis with those from strong lens models. An issue for strong lens modeling for this cluster has been the uncertainty of the mass centroid, because the naked cusp configuration poorly constrains the center of the mass distribution (Inada et al. 2006; Oguri et al. 2008). Given that the measurement of the X-ray centroid agrees well with the location of one of the brightest cluster galaxies (galaxy G2), it now seems safe to assume that the centroid coincides with galaxy G2. We fit the positions of the three quasar images assuming an NFW profile plus

external shear model using the software *glafic* (Oguri 2010). We find that the best-fit model predicts the Einstein radius of  $\theta_E = 18''.3$  for the source redshift of  $z_s = 2.197$ . This translates into a cylindrical cluster mass of  $M_{2D}(< 122\text{kpc}) = 9.30 \times 10^{13} M_\odot$ , which is in good agreement with the enclosed mass derived from the X-ray data (see Figure 6).

## 4. Quasar images

### 4.1. X-ray properties

Given the small  $1''.8$  image separation of images B and C (see Figure 7), we measure the X-ray fluxes and spectra of the quasar images using a circular aperture with a radius of  $0''.9$  for all the quasar images. The observed counts in the 0.5–7 keV band are 687, 1073, and 295, for images A–C, respectively. The net contamination from the background and the cluster is estimated to be only a few percent. Similarly the contamination from image B in the extraction radius for image C is estimated to be  $\sim 10$  counts, which is smaller than the  $1\sigma$  statistical error of the flux of image C. We do not find any clear sign of time variability for light curves produced with time resolutions of 2048 or 4096 s.

The combined spectrum of the three lensed images A, B, and C is shown in the left panel of Figure 8. We fit the spectrum with a power-law model. The Galactic absorption is again fixed at  $N_H = 1.67 \times 10^{20} \text{cm}^{-2}$ . We do not find significant intrinsic absorption in the total spectrum. The power-law model is acceptable at the 90% confidence level ( $\chi^2/\text{dof} = 57.1/63$ ) and the power-law index of  $\Gamma = 1.55 \pm 0.06$  agrees well with the mean value for mini-BAL quasars observed with *Chandra* (Gibson et al. 2009). The corresponding total luminosity is  $5.3 \times 10^{45} \text{ ergs s}^{-1}$  in the 2–10 keV band. We do not detect any significant emission from the neutral iron  $K\alpha$  line at 2.0 keV in the observed frame (or 6.4 keV in the rest frame). The 90% upper limit on the equivalent width is  $\text{EW} < 170 \text{ eV}$  in the quasar

rest frame for a power-law combined with a Gaussian line model at 2 keV.

Next we study the spectra of the individual quasar images. We first check the hardness ratios defined by the count rate ratio in the 2–7 keV and 0.5–2 keV bands. The result indicates that a spectral shape of image C differs from A and B because the hardness ratio for image C ( $0.48 \pm 0.06$ ) differs from those of images A ( $0.37 \pm 0.03$ ) and B ( $0.36 \pm 0.02$ ). Indeed, the spectra of images A–C plotted in the right panel of Figure 8 clearly indicate that the emission of image C is heavily absorbed in the soft band. To quantify this, we fit the spectrum with a power-law model absorbed by intervening cold material in addition to the Galactic interstellar medium. Since the location of the cold absorber is not known, we consider cases with the absorber located at either the quasar redshift of  $z_s = 2.197$  or at the lens redshift of  $z_l = 0.584$ .

The result of the power-law plus the absorption model fits are summarized in Table 5. While the inclusion of the additional absorption does not improve the best-fit  $\chi^2$  value for images A and B, the fits to image C are significantly improved by including the absorption. We find that the improvement is significant at the  $> 99.98\%$  confidence level according to the F-test ( $\Delta\chi^2 = 11$  for one additional parameter), although the redshift of the absorber is not constrained. We also tried a simultaneous fit to the three spectra with a common intrinsic spectral index  $\Gamma$ , because the intrinsic photon indices are statistically consistent among the three images. The result shown in Table 6 again indicates that the extra absorption is significant only for image C.

## 4.2. Comparison with optical and radio flux ratios

In Table 7, we compare flux ratios between quasar images measured in the *Chandra* X-ray images with radio and optical flux ratios presented in Kratzer et al. (2011). We

find that the absorption corrected flux ratio  $C/B$  in X-ray is larger than the optical flux ratios and is close to the radio flux ratio. We note that the optical  $C/B$  flux ratio becomes  $C/B \sim 0.4$  once the dust extinction is corrected (see below), which is also consistent with the radio and absorption-corrected X-ray flux ratios. The nearly consistent flux ratios between the radio, optical, and X-ray observations imply that microlensing effect is not significant for this system, particularly because X-ray flux ratios are more easily affected by microlensing (e.g., Ota et al. 2006b; Pooley et al. 2007; Dai et al. 2010).

The origin of the absorption may be inferred from the dust-to-gas ratio. Based on the optical spectra of images B and C in Oguri et al. (2008), we estimated a color excess of  $E(B - V) \simeq 0.07$  for absorption at  $z_s = 2.197$  and  $E(B - V) \simeq 0.17$  for absorption at  $z_l = 0.584$ . These imply dust-to-gas ratios of  $E(B - V)/N_H \simeq 2 \times 10^{-24} \text{mag cm}^2$  and  $E(B - V)/N_H \simeq 3 \times 10^{-23} \text{mag cm}^2$  at the source and lens redshifts, respectively. The higher value found for dust in the lens is broadly consistent with measurements for other lens systems (Dai & Kochanek 2009), while the value for dust at the source redshift is much lower than expected from this observed correlation. However, such low dust-to-gas ratios appear to be common for intrinsic absorption features of quasars (Hall et al. 2006), which can be explained by dust evaporation due to irradiation by the central source. Thus we cannot draw any firm conclusion about the origin of the absorption from this analysis. Both the mini-BAL features in the quasar spectrum (see Oguri et al. 2008) and the deficiency of dust in the intracluster medium particularly near the center (Chelouche et al. 2007; Muller et al. 2008; Bovy et al. 2008; Kitayama et al. 2009) suggest that intrinsic absorption at the quasar redshift is the more likely scenario, although the anomalous flux ratios imply a faint galaxy near image C which might host the dust at the lens redshift. If the former interpretation is correct, the different absorptions between image B and C probe spatial variations of the absorption content, possibly related to the structure of disk wind outflows (Green 2006).

## 5. Summary and Discussions

We have presented results from *Chandra* observations of SDSS J1029+2623, the largest-separation gravitational lens system, produced by a cluster of galaxies at  $z = 0.58$ . We detect significant X-ray emission from the lensing cluster as well as three lensed quasar images.

From the extended cluster emission, the X-ray temperature and bolometric luminosity are constrained to be  $kT = 8.1_{-1.2}^{+2.0}$  keV and  $L_X = 9.6 \times 10^{44}$  erg s $^{-1}$ , which is consistent with the luminosity-temperature relation of distant clusters. While the estimated cooling time is shorter than the Hubble time, the lack of a significant temperature drop at the cluster center suggests that radiative cooling is not important in this system. From the image analysis, we have found that the cluster emission is elongated along the East-West direction and has a subpeak in the North-West region. This indicates that the system has undergone a merger. However, the modest ellipticity of the gas distribution found in the main cluster component indicates that the irregularity of mass distribution may not be large. We have reconstructed the mass profile of the lensing cluster, assuming isothermality and hydrostatic equilibrium to find that the X-ray mass within the Einstein radius or  $\sim 120$  kpc is in a good agreement with that expected from the strong lensing. The result further supports the idea that there is not any significant departure from the equilibrium state in the cluster core.

The X-ray spectra of the three quasar images above 2 keV are well represented by a power-law with a photon index of  $\Gamma \sim 1.55$  that is typical of mini-BAL quasars. However, significant soft X-ray absorption due to the cold material is detected only in image C. After correcting for the X-ray absorption, the X-ray flux ratios between the quasar images are roughly consistent with those in optical and radio, which suggests that microlensing is not significant for this system. This indicates that the flux ratio anomaly seen in this lens system has to be due to substructure (see, e.g., Kochanek & Dalal 2004). It is difficult to

distinguish the possibilities between absorbers at the quasar redshift and at the cluster redshifts from the X-ray spectrum or the dust-to-gas ratio.

Both the surface brightness profile of the lensing cluster and the anomalous flux ratio are better understood by comparing the result with accurate mass modeling results obtained from gravitational lensing analysis. For this purpose we have recently obtained *Hubble Space Telescope* images of this system. Lensing analysis results of the *HST* data and a comparison with the *Chandra* results will be presented in a forthcoming paper.

We thank K. Aoki for useful discussions. This work was supported in part by the Grant-in-Aid for Scientific Research by the Ministry of Education, Culture, Sports, Science and Technology, No.22740124 (N.O.). This work was supported in part by the FIRST program “Subaru Measurements of Images and Redshifts (SuMIRe)”, World Premier International Research Center Initiative (WPI Initiative), MEXT, Japan, and Grant-in-Aid for Scientific Research from the JSPS (23740161). C.S.K. is supported by NSF grant AST-1009756. X.D. acknowledges support by NASA/SAO fund GO0-11147B. T.S. acknowledges support from NSF through grant AST-0444059-001 and the Smithsonian Astrophysics Observatory through grant GO0-11147A.

*Facilities:* CXO (ACIS).

## REFERENCES

- Arnaud, M., Pratt, G. W., Piffaretti, R., Böhringer, H., Croston, J. H., & Pointecouteau, E. 2010, *A&A*, 517, A92
- Bovy, J., Hogg, D. W., & Moustakas, J. 2008, *ApJ*, 688, 198
- Chelouche, D., Koester, B. P., & Bowen, D. V. 2007, *ApJ*, 671, L97
- Clowe, D., et al. 2006, *ApJ*, 648, L109
- Dai, X., & Kochanek, C. S. 2009, *ApJ*, 692, 677
- Dai, X., Kochanek, C. S., Chartas, G., et al. 2010, *ApJ*, 709, 278
- De Filippis, E., Sereno, M., Bautz, M. W., & Longo, G. 2005, *ApJ*, 625, 108
- Flores, R. A., Allgood, B., Kravtsov, A. V., et al. 2007, *MNRAS*, 377, 883
- Garmire, G.P., Bautz, M.W., Ford, P.G., Nousek, J.A., & Ricker, G.R. 2003, *Proc.SPIE*, 4851, 28
- Gibson, R. R., Brandt, W. N., Gallagher, S. C., & Schneider, D. P. 2009, *ApJ*, 696, 924
- Green, P. J. 2006, *ApJ*, 644, 733
- Hall, P. B., Gallagher, S. C., Richards, G. T., et al. 2006, *AJ*, 132, 1977
- Hashimoto, Y., Böhringer, H., Henry, J. P., Hasinger, G., & Szokoly, G. 2007, *A&A*, 467, 485
- Inada, N., Oguri, M., Pindor, B., et al. 2003, *Nature*, 426, 810
- Inada, N., Oguri, M., Keeton, C. R., et al. 2005, *PASJ*, 57, L7
- Inada, N., et al. 2006, *ApJ*, 653, L97



- Kalberla, P. M. W., Burton, W. B., Hartmann, D., Arnal, E. M., Bajaja, E., Morras, R.,  
Pöppel, W. G. L. 2005, *A&A*, 440, 775
- Kawahara, H. 2010, *ApJ*, 719, 1926
- Kitayama, T., et al. 2009, *ApJ*, 695, 1191
- Kochanek, C. S., & Dalal, N. 2004, *ApJ*, 610, 69
- Kratzer, R. M., Richards, G. T., Goldberg, D. M., et al. 2011, *ApJ*, 728, L18
- Lamer, G., Schwope, A., Wisotzki, L., & Christensen, L. 2006, *A&A*, 454, 493
- Lau, E. T., Nagai, D., Kravtsov, A. V., Vikhlinin, A., & Zentner, A. R. 2012, *arXiv:1201.2168*
- Li, G. L., Mao, S., Jing, Y. P., Lin, W. P., & Oguri, M. 2007, *MNRAS*, 378, 469
- Markevitch, M., Ponman, T. J., Nulsen, P. E. J., et al. 2000, *ApJ*, 541, 542
- Minor, Q. E., & Kaplinghat, M. 2008, *MNRAS*, 391, 653
- Muller, S., et al. 2008, *ApJ*, 680, 975
- Nakamura, T. T., & Suto, Y. 1997, *Prog. Theor. Phys.*, 97, 49
- Navarro, J. F., Frenk, C. S., & White, S. D. M. 1997, *ApJ*, 490, 493
- Oguri, M. 2010, *PASJ*, 62, 1017
- Oguri, M., & Keeton, C. R. 2004, *ApJ*, 610, 663
- Oguri, M., et al. 2004, *ApJ*, 605, 78
- Oguri, M., et al. 2008, *ApJ*, 676, L1
- Oguri, M., Bayliss, M. B., Dahle, H., Sharon, K., Gladders, M. D., Natarajan, P., Hennawi,  
J. F., & Koester, B. P. 2012, *MNRAS*, in press (*arXiv:1109.2594*)

- Ota, N., Inada, N., Oguri, M., et al. 2006, ApJ, 647, 215
- Ota, N., Kitayama, T., Masai, K., & Mitsuda, K. 2006, ApJ, 640, 673
- Ota, N., Pointecouteau, E., Hattori, M., & Mitsuda, K. 2004, ApJ, 601, 120
- Owers, M. S., Nulsen, P. E. J., Couch, W. J., & Markevitch, M. 2009, ApJ, 704, 1349
- Pooley, D., Blackburne, J. A., Rappaport, S., & Schechter, P. L. 2007, ApJ, 661, 19
- Sharon, K., Ofek, E. O., Smith, G. P., et al. 2005, ApJ, 629, L73
- Smith, R. K., Brickhouse, N. S., Liedahl, D. A., & Raymond, J. C. 2001, ApJ, 556, L91
- Suto, Y., Sasaki, S., & Makino, N. 1998, ApJ, 509, 544

Table 1: APEC Models of the Overall Spectrum

Parameter	Value (90% error)
$N_{\text{H}}$ ( $\text{cm}^{-2}$ )	$1.67 \times 10^{20}$ (F)
$kT$ (keV)	8.1 (6.8 – 10.1)
Abundance ( $Z_{\odot}$ )	0.22(< 0.44)
Redshift	0.584 (F)
Normalization <sup>a</sup>	$7.31$ ( $6.93 - 7.68$ ) $\times 10^{-4}$
$\chi^2/dof$	47.5/45
$f_{\text{X},0.5-7}$ ( $\text{erg s}^{-1} \text{cm}^{-2}$ ) <sup>b</sup>	$4.6 \times 10^{-13}$
$L_{\text{X},0.5-7}$ ( $\text{erg s}^{-1}$ ) <sup>c</sup>	$5.5 \times 10^{44}$
$L_{\text{X,bol}}$ ( $\text{erg s}^{-1}$ ) <sup>d</sup>	$9.6 \times 10^{44}$

<sup>a</sup>Normalization factor for the APEC model,  $\int n_e n_H dV / 4\pi D_A^2 (1+z)^2$  in  $10^{-14} \text{cm}^{-5}$ , where  $D_A$  is angular size distance to the cluster.

<sup>b</sup>Galactic absorption-corrected X-ray flux in the 0.5–7 keV band within  $r < 1'$ .

<sup>c</sup>Galactic absorption-corrected X-ray luminosity in the 0.5–7 keV band within  $r < 1'$ .

<sup>d</sup>Bolometric luminosity within  $r_{500}$ .

(F) Fixed parameters.

Table 2. Results for Circularly Symmetric Models

Model	Parameter	Value
$\beta$ -model	$S_0$ (counts s <sup>-1</sup> cm <sup>-2</sup> kpc <sup>-2</sup> ) <sup>a</sup>	$3.57^{+0.28}_{-0.26} \times 10^{-9}$
	$\beta$	$0.72^{+0.05}_{-0.04}$
	$r_c$ (arcsec/kpc)	$16.4^{+1.8}_{-1.6}/109^{+12}_{-11}$
	$\chi^2/dof$	183.2/196
NFW-SSM model	$S_0$ (counts s <sup>-1</sup> cm <sup>-2</sup> kpc <sup>-2</sup> ) <sup>a</sup>	$4.03^{+0.31}_{-0.39} \times 10^{-9}$
	$B$	$12.2^{+1.6}_{-1.2}$
	$r_s$ (arcsec/kpc)	$78^{+16}_{-11}/519^{+104}_{-77}$
	$\chi^2/dof$	178.9/196

Table 3. Results for Elliptical Models

Model	Parameter	Value
Single elliptical $\beta$ -model	$x_{0,1}, y_{0,1}$	10:29:12.395, +26:23:33.71 <sup>a</sup>
	$S_0$ (counts s <sup>-1</sup> cm <sup>-2</sup> kpc <sup>-2</sup> )	$3.57^{+0.28}_{-0.25} \times 10^{-9}$
	$\beta$	$0.70^{+0.04}_{-0.03}$
	$r_c$ (arcsec/kpc)	$17.6^{+1.7}_{-1.6}/118^{+12}_{-10}$
	$\epsilon$	$0.214^{+0.034}_{-0.035}$
	$\theta$	$0.36^{+0.09}_{-0.09}$
Double elliptical $\beta$ -model	$x_{0,1}, y_{0,1}$	10:29:12.471, +26:23:33.24 <sup>b</sup>
	$S_{0,1}$ (counts s <sup>-1</sup> cm <sup>-2</sup> kpc <sup>-2</sup> )	$3.15^{+0.36}_{-0.61} \times 10^{-9}$
	$\beta_1$	$0.71^{+0.04}_{-0.04}$
	$r_{c,1}$ (arcsec/kpc)	$19.0^{+2.4}_{-1.9}/127^{+16}_{-13}$
	$\epsilon_1$	$0.214^{+0.034}_{-0.035}$
	$\theta_1$	$0.36^{+0.09}_{-0.09}$
	$x_{0,2}, y_{0,2}$	10:29:11.853, +26:23:37.37 <sup>c</sup>
	$S_{0,2}$ (counts s <sup>-1</sup> cm <sup>-2</sup> kpc <sup>-2</sup> )	$3.1^{+2.3}_{-1.2} \times 10^{-9}$
	$\beta_2$	0.70(F)
	$r_{c,2}$ (arcsec/kpc)	$3.9^{+4.1}_{-1.7}/26^{+28}_{-12}$
	$\epsilon_2$	0.19(< 0.35)
	$\theta_2$	0.0(F)

<sup>a</sup>The 90% errors are  $\pm 1''.1$  for  $x_0$  and  $\pm 1''.0$  for  $y_0$ .

<sup>b</sup>The 90% errors are  $\pm 1''.4$  for  $x_{0,1}$  and  $\pm 1''.1$  for  $y_{0,1}$ .

<sup>c</sup>The 90% errors are  $\pm 1''.7$  for  $x_{0,2}$  and  $\pm 1''.5$  for  $y_{0,2}$ .

Table 4: Masses for Different Critical Overdensities

Model	$M_{\text{vir}}^{\text{a}}$	$r_{\text{vir}}^{\text{b}}$	$M_{500}^{\text{a}}$	$r_{500}^{\text{b}}$	$M_{1000}^{\text{a}}$	$r_{1000}^{\text{b}}$	$M_{2500}^{\text{a}}$	$r_{2500}^{\text{b}}$
$\beta$	$12.95^{+5.00}_{-3.07}$	$2.10^{+0.24}_{-0.18}$	$6.68^{+2.60}_{-1.59}$	$1.09^{+0.13}_{-0.09}$	$4.65^{+1.83}_{-1.11}$	$0.77^{+0.09}_{-0.07}$	$2.81^{+1.13}_{-0.68}$	$0.48^{+0.06}_{-0.04}$
NFW-SSM	$15.67^{+6.55}_{-3.93}$	$2.24^{+0.28}_{-0.21}$	$9.28^{+3.93}_{-2.41}$	$1.22^{+0.15}_{-0.12}$	$6.45^{+2.81}_{-1.72}$	$0.86^{+0.11}_{-0.08}$	$3.52^{+1.62}_{-0.99}$	$0.52^{+0.07}_{-0.05}$

---

<sup>a</sup>In units of  $10^{14}M_{\odot}$ .

<sup>b</sup>In units of Mpc.

Table 5: Absorbed Power-law Models for the Quasar Images

Name	No extra absorption		Absorption at $z = 2.197$			Absorption at $z = 0.584$		
	$\Gamma$	$\chi^2/\text{dof}$	$\Gamma$	$N_{\text{H}}^{\text{a}}$	$\chi^2/\text{dof}$	$\Gamma$	$N_{\text{H}}^{\text{a}}$	$\chi^2/\text{dof}$
A	$1.56^{+0.12}_{-0.11}$	31.3/33	$1.56^{+0.16}_{-0.11}$	$0.00(< 0.70)$	31.3/32	$1.56^{+0.16}_{-0.11}$	$0.00(< 0.12)$	31.3/32
B	$1.68^{+0.09}_{-0.09}$	23.2/33	$1.68^{+0.10}_{-0.09}$	$0.00(< 0.33)$	23.2/32	$1.68^{+0.10}_{-0.09}$	$0.00(< 0.06)$	23.2/32
C	$1.21^{+0.14}_{-0.14}$	25.1/25	$1.68^{+0.32}_{-0.28}$	$3.13^{+2.24}_{-1.68}$	13.5/24	$1.71^{+0.34}_{-0.30}$	$0.54^{+0.40}_{-0.30}$	14.1/24
Total	$1.55^{+0.06}_{-0.06}$	57.1/63	$1.55^{+0.10}_{-0.06}$	$0.00(< 0.46)$	57.1/62	$1.55^{+0.10}_{-0.06}$	$0.00(< 0.08)$	57.1/62

<sup>a</sup>The hydrogen column density in the unit of  $[10^{22} \text{ cm}^{-2}]$ .

Table 6: Joint fits to the Quasar Spectra

Name	Absorption at $z = 2.197$			Absorption at $z = 0.584$		
	$\Gamma$	$N_{\text{H}}^{\text{a}}$	$\chi^2/\text{dof}$	$\Gamma$	$N_{\text{H}}^{\text{a}}$	$\chi^2/\text{dof}$
A	$1.65^{+0.08}_{-0.08}$	$0.24(< 0.89)$	69.4/90	$1.65^{+0.08}_{-0.08}$	$0.04(< 0.15)$	70.0/90
B		$0.00(< 0.25)$			$0.00(< 0.04)$	
C		$2.97^{+1.38}_{-1.08}$			$0.49^{+0.22}_{-0.18}$	

<sup>a</sup>The hydrogen column density in the unit of  $[10^{22} \text{ cm}^{-2}]$ .



Table 7. X-ray and optical properties of SDSS J1029+2623

Name	$F_X^{a,b}$	hardness <sup>c</sup>	$\alpha_{\text{ox}}$	$f(\text{X})^{b,d}$	$f(\text{opt}, V)^d$	$f(\text{opt}, I)^d$	$f(\text{radio})^d$
A	$0.90 \pm 0.03$ (0.89)	$0.37 \pm 0.03$	−1.32	0.66 (0.64)	0.96	0.95	$0.80 \pm 0.06$
B	$1.37 \pm 0.04$ (1.34)	$0.36 \pm 0.02$	−1.26	$\equiv 1$	$\equiv 1$	$\equiv 1$	$\equiv 1$
C	$0.49 \pm 0.03$ (0.40)	$0.48 \pm 0.06$	−1.14	0.36 (0.27)	0.16 <sup>e</sup>	0.24 <sup>e</sup>	$0.46 \pm 0.05$

<sup>a</sup>Absorption-corrected, 0.5–7 keV X-ray flux in units of  $10^{-13} \text{erg s}^{-1} \text{cm}^{-2}$  and the 1- $\sigma$  error.

<sup>b</sup>The value in the parenthesis are those without absorption corrections.

<sup>c</sup>Hardness ratios defined by the count rate ratios in 2 – 7 keV and 0.5 – 2 keV bands. Errors indicate 68% confidence limits.

<sup>d</sup>Flux normalized by the flux of image B. The optical and radio flux ratios are taken from Kratzer et al. (2011). Statistical errors on the optical flux ratios are  $\lesssim 2\%$  (Oguri et al. 2008).

<sup>e</sup>The optical  $C/B$  flux ratio becomes  $C/B \sim 0.4$  once the dust extinction is corrected.

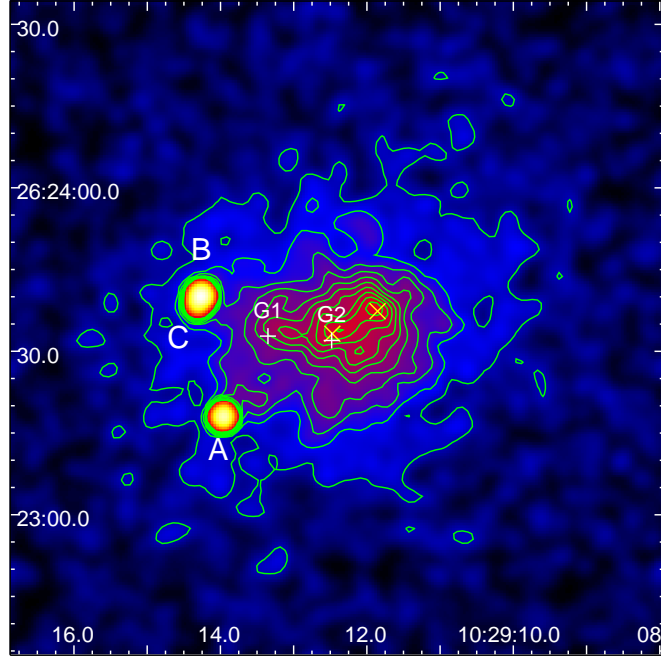


Fig. 1.— Adaptively-smoothed ACIS-S3 image of SDSS J1029+2623 in the 0.5–7 keV band. The A–C quasar images of SDSS J1029+2623 and the extended emission from the lensing cluster are seen. The X-ray centroid of the cluster component and the North-West subpeak are marked with an “x” while the positions of the two most luminous galaxies, G1 and G2, are marked with a “+”. The close B/C image pair is resolved in the raw, unsmoothed image (see §4).

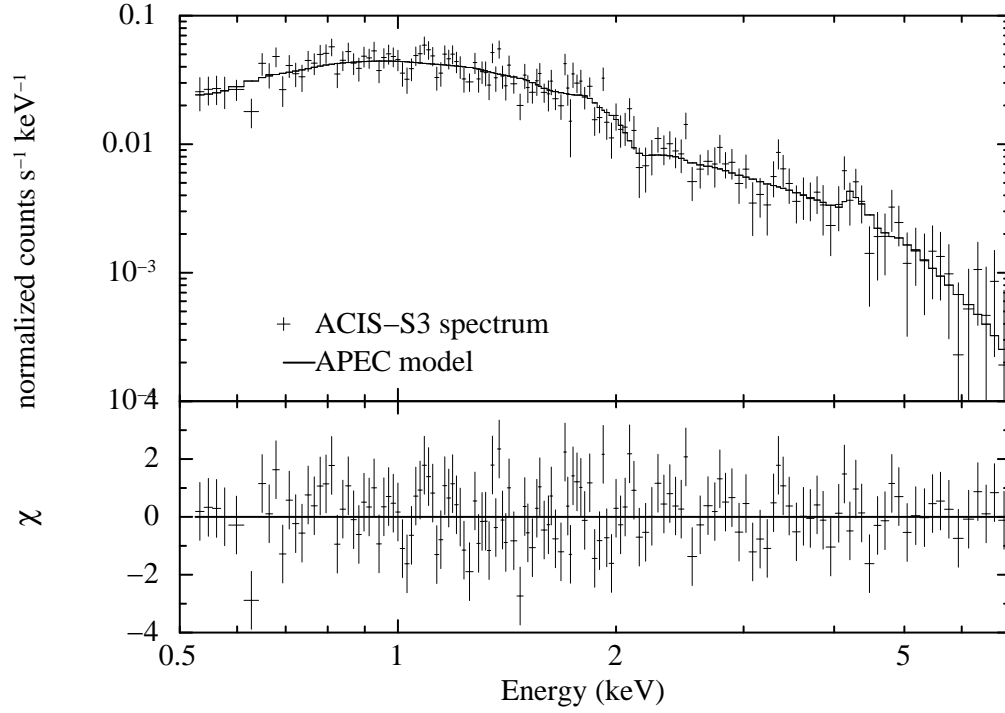


Fig. 2.— *Chandra* ACIS-S3 spectrum of SDSS J1029+2623 ( $r < 1'$ ) fitted with the APEC model. In the top panel, the crosses denote the observed spectrum and the histogram function shows the best-fit model convolved with the telescope and detector response functions. The bottom panel shows the residuals of the fit in units of  $\sigma$ .

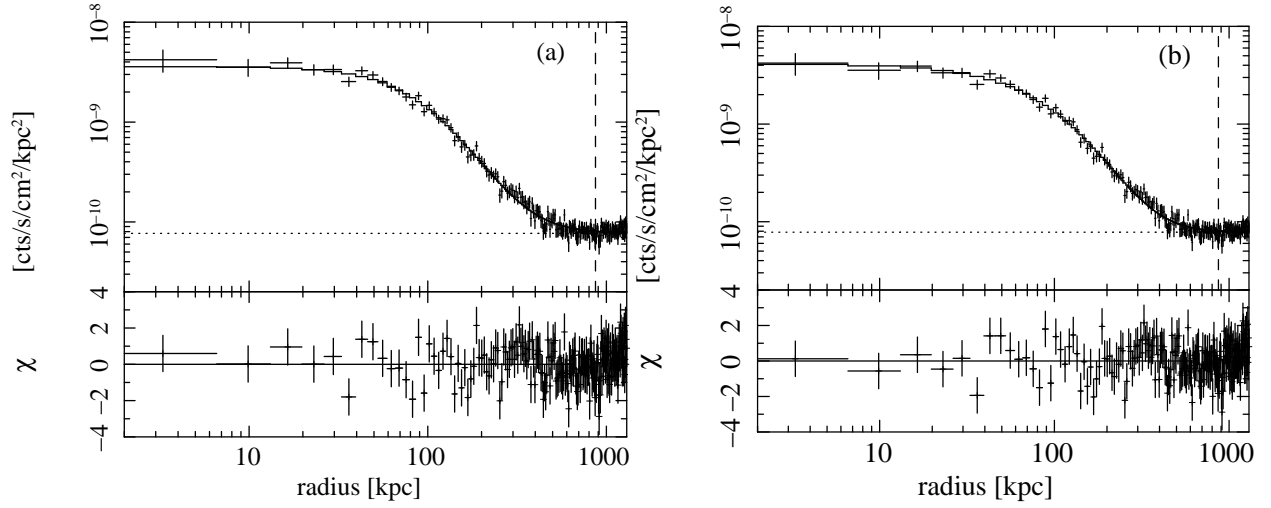


Fig. 3.— Results of the X-ray surface brightness profile fits with (a) the  $\beta$ -model and (b) the NFW-SSM model. In each panel, the crosses show the observed surface brightness in the 0.5–5 keV band and the solid line shows the best-fit model. The background is shown with the horizontal dotted line. The vertical dashed line shows the observed extent of the diffuse X-ray emission,  $r_X$  (see text). The bottom panel shows the residuals in units of the local noise.

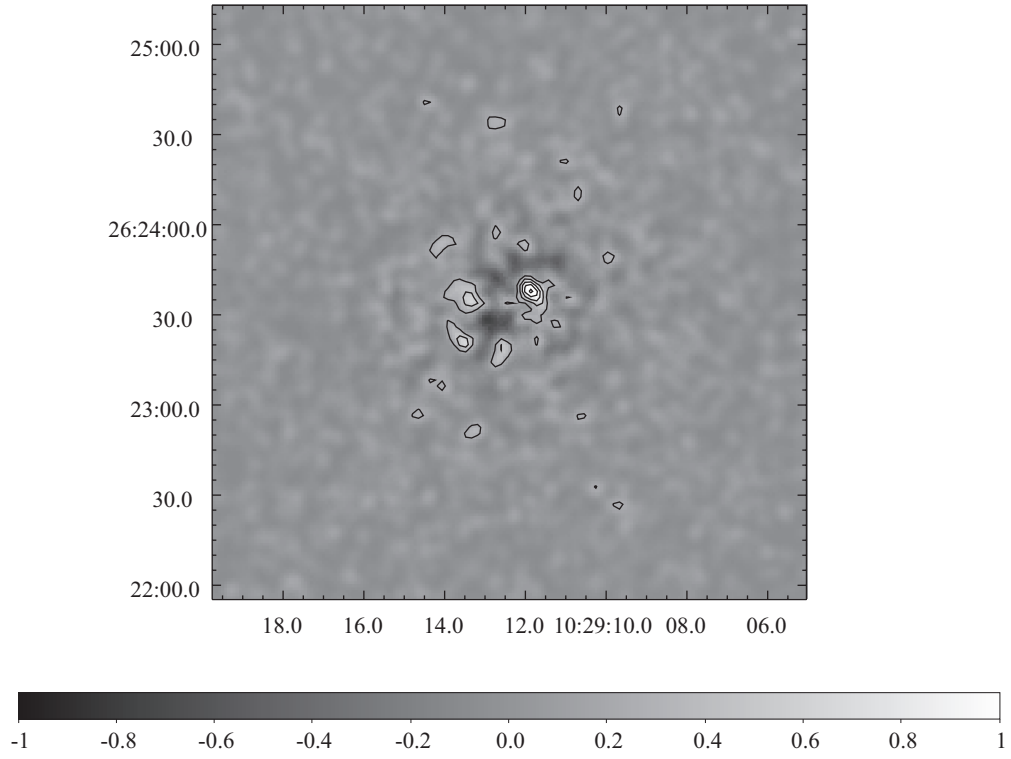


Fig. 4.— Residuals from fits with a single elliptical  $\beta$ -model. The image is smoothed with a  $\sigma = 2''$  Gaussian, and excess emission over the best-fit model is shown by the black contours with linear spacing.

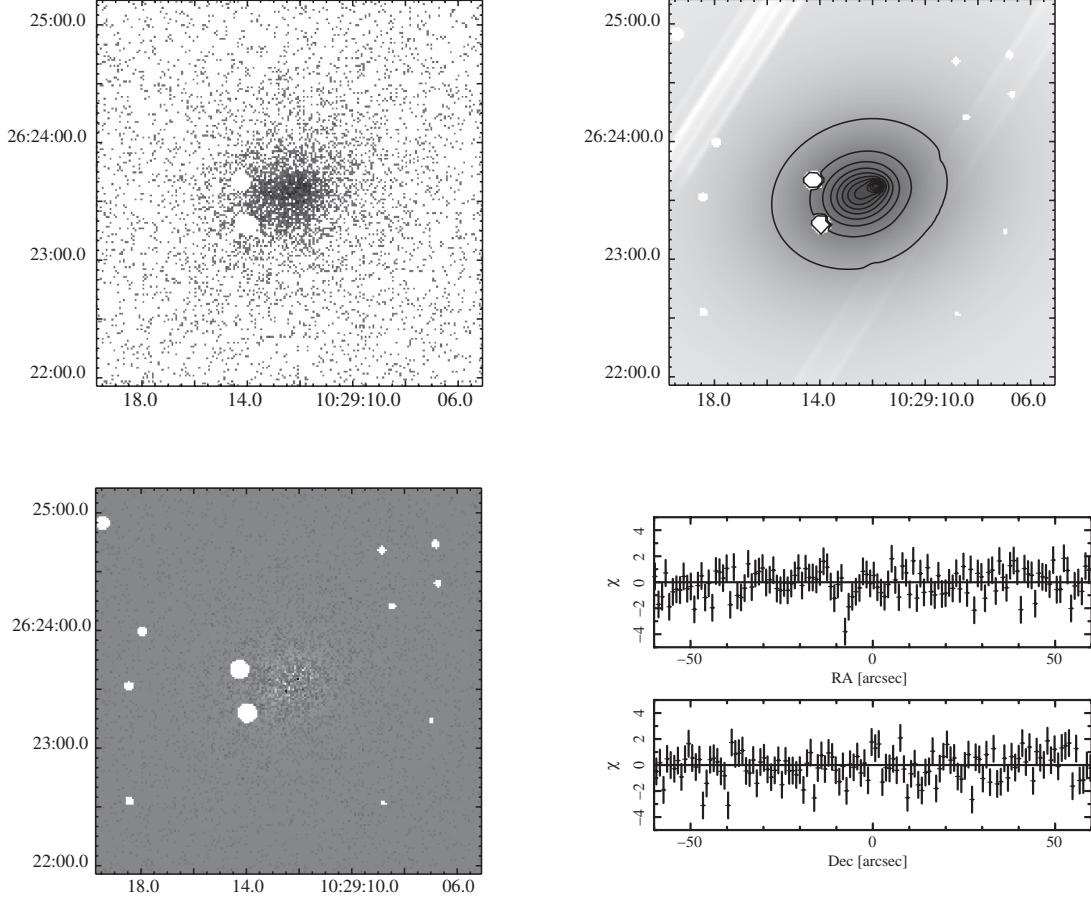


Fig. 5.— Results for the fits with the double elliptical  $\beta$ -model. Top left: *Chandra* ACIS-S3 image of the central  $3'.3 \times 3'.3$  region of SDSS J1029+2623 in the 0.5–5 keV energy range. Top right: The best-fitting elliptical  $\beta$ -model, overlaid with logarithmically spaced intensity contours. Bottom left: Residuals from the fit. Bottom right: Residuals along East-West (*top*) and North-South (*bottom*) lines through the cluster center in units of significance.

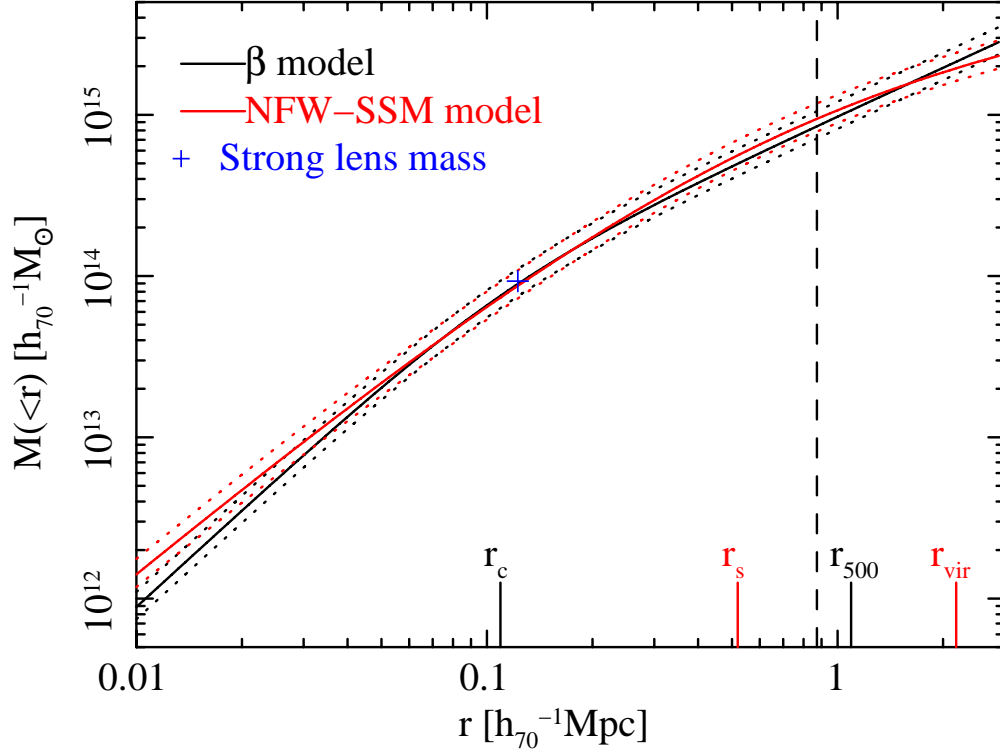


Fig. 6.— Enclosed mass of the lensing cluster,  $M_X$ , for the  $\beta$ -model (black) and the NFW-SSM model (red). The dotted lines indicate the 90% error ranges. Note that  $M_X$  is a cylindrical cluster mass projected within a radius  $r$ . The mass derived from gravitational lensing is also shown for comparison. The meaning of the vertical dashed line is the same as Figure 3.

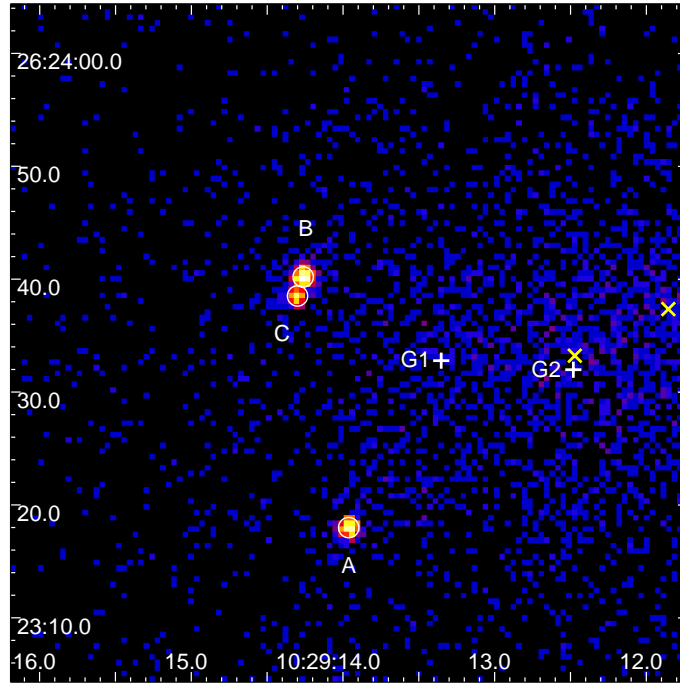


Fig. 7.— Raw ACIS-S3 image of SDSS J1029+2623 in the 0.5–7 keV band. The spectral regions for quasar images A–C are indicated with the circles. The meaning of the labels are the same as Figure 1.



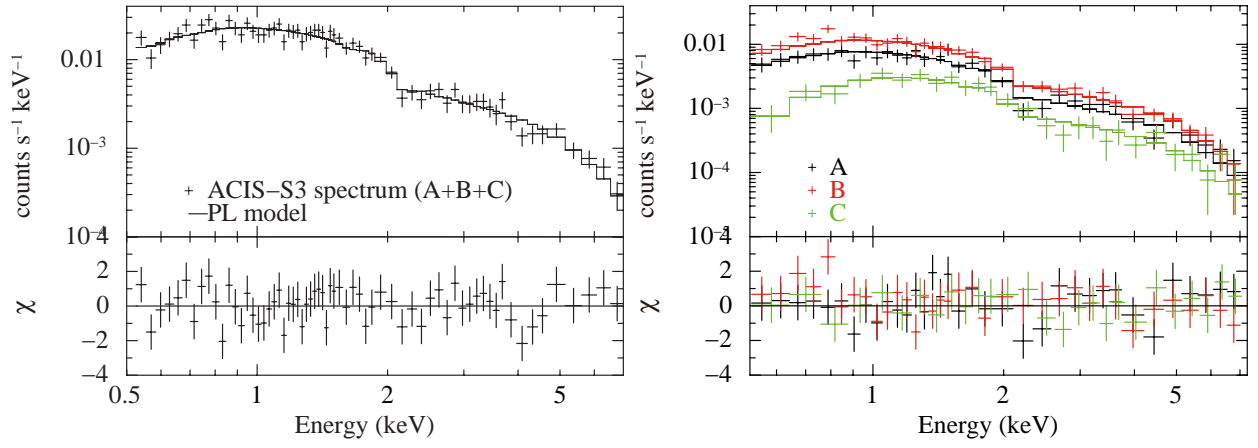


Fig. 8.— Left: total quasar spectrum fit with the power-law model (solid line). Right: Spectra of lensed quasar images A (black), B (red), and C (green) fit with a common intrinsic slope  $\Gamma$ .